Modeling multicomponent reactive membranes

Olga Kuksenok* and Anna C. Balazs
Chemical Engineering Department, University of Pittsburgh, Pittsburgh, Pennsylvania 15261, USA
(Received 8 January 2007; published 9 May 2007)

Using analytical calculations and computer simulations, we study binary *AB* and ternary *ABC* membranes that respond to an external stimulus by interconverting *A* and *B* components. The *C* component is assumed to be nonreactive and is incompatible with both *A* and *B*. We also assume that *A* and *B* have different spontaneous curvatures. The dynamics of the ternary system is described in terms of three order parameters: two specify the local composition and a third characterizes the local height of the membrane. Our description of the two-component membrane is based on a recent model proposed by Reigada *et al.* [Phys. Rev. E. **72**, 051921 (2005)]; we extend the latter approach by explicitly including the effects of the membrane's surface tension on the phase behavior of the system. By performing a linear stability analysis, we determine the behavior of the reactive *AB* membrane for a given bending elasticity and surface tension at different values of the reaction rate coefficients. We also numerically integrate the governing dynamic equations, and the results of these simulations are in agreement with the analytical predictions. For the two-component membranes, we calculate two critical values of the reaction rate coefficients, which define the behavior of the system, and plot the phase diagrams in terms of different parameters. We illustrate that the surface tension of the membrane strongly affects these critical values of the reaction rate coefficients and therefore the location of the phase boundaries. We also pinpoint the regions on the phase diagram where the late-time behavior is affected by the initial fluctuations, i.e., where such a reactive system has some "memory" of its prior state. In the case of the three-component system, we show that the presence of the nonreactive *C* component strongly affects the composition and topology of the membrane, as well as critically altering the propagation of the traveling waves within the system.

DOI: 10.1103/PhysRevE.75.051906 PACS number(s): 87.16.Dg, 64.75.+g, 82.40.Ck, 82.45.Mp

I. INTRODUCTION

The chemical heterogeneity and physical diversity inherently present in biological membranes contribute to their amazingly rich, nonequilibrium dynamical behavior. In turn, this complex dynamical behavior controls a variety of functions, such as signaling, molecular recognition, and transport. Theoretical and computational modeling allows us to develop a greater understanding of various processes that characterize the dynamics of these membranes—from specific reactions and diffusion processes within the membrane to the interaction between the membrane and the surrounding solutions—and to predict the response of the membrane to the external stimuli. By isolating critical factors that contribute to specific dynamic behavior in biological membranes, theoretical studies can also provide design rules for creating biomimetic, synthetic membranes. In particular, studies into the kinetic aspects of self-assembly and various functions in lipid membranes can lead to designing new classes of materials that are capable of performing advanced technological functions [1], such as dynamic restructuring due to external stimuli, self-replication, or self-healing.

In the current work, we use theoretical and computational modeling to examine the nonequilibrium dynamics of model, reactive membranes. To control the dynamics of reactive membranes, one can potentially utilize various external stimuli (e.g., light or a flux of external reactants) to alter the rates of reactions that are occurring within the system. Herein, we focus on establishing guidelines for harnessing such stimuli to drive the membranes to perform specific functions, such as dynamic restructuring or "sensing" and responding to concentration gradients within the system. In spite of the significant progress that has been made in understanding the behavior of both biological and synthetic membranes [2,3], the nonequilibrium dynamics of such reactive membranes has received considerably less attention. Research relevant to our efforts includes work by John and Bar [4], who used mathematical modeling to study the interplay between a number of kinetic processes, including the phase separation between proteins and lipids and the attachment and detachment of proteins to and from the lipid membrane in the presence of regulating enzymes. They showed [4] that, for sufficiently high enzymatic activity, traveling domains of lipids and proteins could appear in the system. Such traveling domains allow the membrane to undergo a faster restructuring and to respond to spatial gradients in the environment.

In the above example, the multicomponent reactive membrane was considered to be flat. Here, we are interested in the situation where both the composition and the shape (curvature) of the membrane can be controlled dynamically (via, for example, external light source or flux of the reactants in the outside solution). A number of studies [5–10] showed that different active inclusions (such as proteins), which are localized in the membrane, could directly affect the shape of the membrane. Moreover, such proteins can be activated by external light [6] and thus the external stimuli can be used to dynamically control the shape of the membrane. Finally, Petrov *et al.* [11] showed experimentally that the magnitude and the sign of the membrane's curvature can be controlled

*Email address: kuksenok@dorothy.che.pitt.edu

by photoinduced chemical reactions in bulk aqueous solutions.

With respect to the theoretical modeling of reactive multicomponent membranes, Reigada *et al.* [12] introduced a phenomenological description of a reactive bilayer in which two differently shaped components *A* and *B* undergo an externally controlled interconversion reaction. The fact that the *A* and *B* lipids have different shapes results in different curvatures of the *A* and *B* domains. They showed that, in the case where the *A* and *B* components phase separate, the bilayer forms stationary patterns of spatially different composition and curvature; the characteristic length scale of such patterns is defined by the reaction rate coefficient for the interconversion of the *A* and *B* components. Later, the same researchers [13] introduced a more sophisticated approach in which they also assumed that the reaction process actively affects the curvature of the membrane. Such a direct coupling of the external reaction to the local curvature resulted in the generation of traveling waves within the reactive bilayer.

In this work, we study two- and three-component membranes in which an external stimulus initiates a chemical reaction that interconverts two of the components, *A* and *B*. The third component *C* is assumed to be nonreactive and is incompatible with the *A* and *B* components, which have specified spontaneous curvatures. The description of the binary mixture is based on the above model proposed by Reigada *et al.* [13]; we have, however, extended the latter approach by explicitly including the effects of the surface tension of the membrane. As we show below, for the two-component (*AB*) reactive membranes, the phase boundaries within the calculated phase diagrams are highly dependent on the surface tension of the membrane. In addition, we isolate situations where the late-time behavior of the binary system strongly depends on the initial fluctuations, i.e., where such reactive membranes have some "memory" of their prior state. For the three-component reactive membrane, we illustrate how the presence of the nonreactive *C* component affects the dynamical patterns and leads to systems with novel morphologies.

On a fundamental level, the studies of reactive multicomponent membranes can enhance our understanding of the coupling of chemical reactivity, mechanical deformation, and morphological transitions, and reveal rich dynamic behavior that results from a chemomechanical coupling. Furthermore, investigations in this direction could potentially be useful for establishing means of harnessing the conversion of chemical energy into the desired mechanical behavior and, ultimately, the specified morphological transition. Advances in this area can open up new means of driving the self-assembly of multicomponent films into well-defined structures, ranging from well-controlled surface corrugation to more complex three-dimensional objects.

II. THE MODEL

We consider a flexible membrane composed of a ternary *ABC* mixture, where all components are mutually immiscible. The height of the membrane in the z direction, h, is a function of the local composition in the x,y plane, i.e., $h \equiv h(x,y)$; this height is calculated with respect to a flat, undistorted membrane. We assume that, in response to an external stimulus, the *A* and *B* components of the mixture undergo a reversible chemical reaction $A \underset{\Gamma_-}{\overset{\Gamma_+}{\leftrightarrow}} B$, where Γ_+ (Γ_-) is the rate coefficient for the forward (reverse) reaction, and the *C* component is nonreactive. We further assume that the *A* and *B* domains exhibit different spontaneous curvatures. Such membranes could represent a polymeric bilayer and *A* might be a group of lipids, biomolecules, or isomers of an amphiphilic azobenzene derivative that exhibits a particular curvature, while the *B* group displays a dissimilar curvature [12,13]. The *C* component might be any nonreactive group or even an impurity, which does not have spontaneous curvature and is immiscible with the *A* and *B* components. The interconversion reaction between *A* and *B* can be understood, for example, as an isomerizationlike chemical transformation [12,13]. This interconversion reaction changes the local composition of the membrane, and, in addition, can exert a local mechanical force on the membrane, i.e., locally "kick" the membrane, and, therefore, directly modify the local curvature of the layer [13].

We describe the composition of the membrane in terms of two order parameters: $\varphi=\rho_A-\rho_B$ is the difference between the concentrations of the *A* and *B* components within the xy plane, and $\psi=\rho_C$ is the concentration of the *C* component within the x,y plane [14,15]. Following Refs. [12,13], we use the Monge representation and describe the deformation of the membrane in terms of the height field $h(x,y)$, which represents local deviation of the membrane position with respect to the flat, undistorted surface. Such a description is valid for relatively small deformations with respect to the flat surface.

The evolution of the membrane is assumed to be governed by the following set of equations [12–15]:

$$\frac{\partial \varphi}{\partial t} = M_\varphi \nabla^2 \frac{\delta F}{\delta \varphi} - \Gamma \varphi, \tag{1}$$

$$\frac{\partial \psi}{\partial t} = M_\psi \nabla^2 \frac{\delta F}{\delta \psi}, \tag{2}$$

$$\frac{\partial h}{\partial t} = -M_h \frac{\delta F}{\delta h} + \Gamma \varphi \xi, \tag{3}$$

where M_i is the mobility of the ith order parameter. In the above, we assume that the forward and reverse reaction rate coefficients are equal, i.e., $\Gamma \equiv \Gamma_+/2=\Gamma_-/2$. We note that, while Eqs. (1)–(3) represent the first description of such a reactive, three-component membrane, they can be reduced to a number of known limiting cases, as we discuss in detail below.

The form of the free energy functional F is taken to be

$$F(\varphi,\psi,h) = \frac{1}{S_{xy}} \int dx\, dy \left(f_0(\varphi,\psi) + \frac{\sigma}{2}(\nabla h)^2 + \frac{\gamma_\varphi}{2}(\nabla\varphi)^2 + \frac{\gamma_\psi}{2}(\nabla\psi)^2 + \frac{\kappa}{2}(\nabla^2 h - \varphi H_0)^2 \right). \quad (4)$$

S_{xy} here is the surface area of membrane in the x, y plane. The local free energy $f_0(\varphi,\psi)$ in Eq. (4) is chosen to ensure that the mutually immiscible A, B, and C components phase separate [14–16]:

$$f_0(\varphi,\psi) = -a_{20}\varphi^2 + a_{40}\varphi^4 + a_{02}\psi^2 - a_{03}\psi^3 + a_{04}\psi^4 + a_{22}\varphi^2\psi^2. \quad (5)$$

All the coefficients in Eq. (5) are positive (if all three components are immiscible). We determine the actual values of the coefficients a_{ij} in Eq. (5) by requiring the local free energy to have equal minima at $\varphi=\pm 1$, $\psi=0$ [which corresponds to the pure A (B) phase] and $\varphi=0$, $\psi=1$ (which corresponds to the pure C phase). Moreover, we require the local free energy to be symmetric with respect to all three of the components. In particular, we choose [15]

$$a_{40} = 0.5a_{20}, \quad a_{02} = 3a_{20}, \quad a_{03} = 8a_{20}, \quad a_{04} = 4.5a_{20}, \quad a_{22} = 3a_{20}, \quad a_{20} = 0.5. \quad (6)$$

The other important features of the membrane are described by following terms in Eq. (4): the second term expresses the effects of the lateral surface tension of the membrane, the third term details the interfacial tension between the A and B components within the film, and the fourth term details the interfacial tension between the C and A (B) components. Finally, the last term in Eq. (4) specifies the elastic energy of the film due to its rigidity, where κ is the bending modulus [3]. In this last term, we assumed a linear dependence of the local equilibrium curvature on the composition [12], $H_{eq}(\varphi) \equiv \varphi H_0$. With respect to the ternary mixture, this choice for the local curvature ascribes a preferentially flat topology for the C component. In particular, in regions of pure C, $\psi=1$ and $\varphi=0$ [according to Eq. (5)]. Consequently, $H_{eq}(\varphi)\equiv 0$ for pure C domains. Such a scenario constitutes the simplest and the most straightforward case. We note, however, that by modifying the local curvature term in the free energy expression in Eq. (4), the above formalism can be readily adapted to study multicomponent films in which the C component also has a given spontaneous curvature.

Following Reigada *et al.* [13], we take into account that the externally controlled reaction affects not only the local composition, but also the local shape of the film. The effect of the reaction on the local composition is explicitly included through the last term on the right-hand side of Eq. (1). The direct effect of the reaction on the local shape is introduced through the last term in Eq. (3), where ξ is the strength of the latter effect. The local mechanical force exerted on the membrane due to the external reaction is assumed to act in the same direction as the preferred curvature of the product of the reaction [13].

Given the form of the free energy in Eq. (4), we can rewrite Eqs. (1)–(3) as follows:

$$\frac{\partial\varphi}{\partial t} = M_\varphi \nabla^2 \left(\frac{\partial f_0(\varphi,\psi)}{\partial\varphi} - \gamma_\varphi \nabla^2\varphi + \kappa H_0^2\varphi - \kappa H_0 \nabla^2 h \right) - \Gamma\varphi, \quad (7)$$

$$\frac{\partial\psi}{\partial t} = M_\psi \nabla^2 \left(\frac{\partial f_0(\varphi,\psi)}{\partial\psi} - \gamma_\psi \nabla^2\psi \right), \quad (8)$$

$$\frac{\partial h}{\partial t} = M_h \nabla^2 (\sigma h + \kappa\varphi H_0 - \kappa\nabla^2 h) + \Gamma\varphi\xi. \quad (9)$$

Before carrying out a detailed analysis of these equations, we first describe some limiting cases of the above model. If the C component is absent (i.e., the membrane consists of the two reactive components A and B), our model would reduce to the model proposed in Ref. [13], except that we explicitly include the surface tension of the membrane [see the second term in Eq. (4)]. In addition, if the C component is absent and there is no variation in the height of the membrane (i.e., $H_0=0$ and $h\equiv 0$), the above model further reduces to a well-known model for block copolymers [17,18] or reactive polymer blends [19,20]. In this case, the evolution of the reactive AB system is governed solely by the reduced form of Eq. (7), and the morphology of the mixture resembles the lamellar structure formed by microphase-separated, symmetric diblock copolymers [19,20]. And, finally, if all three phase-separating components are present and the A and B components undergo a reversible interconversion, but there is no variation in the height of the film (i.e., $H_0=0$ and $h\equiv 0$), the above model reduces to our recent model of ternary reactive polymer blends [16,21,22].

In the simulation results presented below, we numerically integrate Eqs. (7)–(9) on a square lattice of size 200×200 sites (unless specified otherwise) with a mesh size of $\Delta\equiv 1$ and periodic boundary conditions. We use an explicit finite difference method; to calculate the Laplacian operators, we employ an isotropic discretization, as defined in the cell dynamics method [23]. The latter approach significantly improves the numerical stability of the simulations and allows us to choose a relatively large time step. In the simulations below, we use the time step $\Delta t \equiv 2\times 10^{-2}$, which ensures high numerical accuracy. (We note that we conducted a number of simulations with a time step of $\Delta t \equiv 2\times 10^{-4}$, as well as with a smaller mesh size of $\Delta\equiv 0.5$ and found that the results were identical to those obtained with the chosen time step and mesh size given above.) Unless specified otherwise, we use the following values for the dimensionless parameters for the binary mixture: $M_\varphi=1$, $M_h=1$, $\kappa=0.5$, $H_0=0.2$, $\gamma_\varphi=1$, $\xi=5$ (these values are chosen to be the same as the values in Ref. [13]), and $\sigma=0.05$. For the C component, we set $M_\psi=1/3$ and $\gamma_\psi=3$. We note that the specific choice of $\gamma_\psi=3\gamma_\varphi$ and $M_\psi=M_\varphi/3$ corresponds to ternary mixtures in which the interfacial tensions between A and B, A and C, and B and C (as well as the mobilities of all three different components) are identical (see Ref. [15]).

In the section below, we first conduct a linear stability analysis of the uniform state and illustrate the possible late-time scenarios for membranes composed solely of the A and B components. Then we provide a detailed analysis of the

different states of such binary systems and plot the phase diagrams in the (Γ,ξ) and (Γ,σ) planes. Finally, we consider the three-component ABC membrane and show how the presence of the nonreactive C component affects the evolution of the membrane.

III. RESULTS AND DISCUSSION

A. Linear stability analysis

For the case of AB reactive membranes (where the C component is absent, or $\psi \equiv 0$), the uniform solution for Eqs. (7) and (9) is obtained with $\tilde{h} \equiv 0$ and $\tilde{\varphi} \equiv 0$. (In fact, any arbitrary constant value $\tilde{h} \equiv$const yields a uniform solution; for simplicity, however, we choose the value of $\tilde{h} \equiv 0$ without a loss of generality with respect to the following discussion.) Below, we first define the stability of such a uniform, flat solution for the given system parameters by performing a linear stability analysis. We then compare the analytical predictions obtained from this linear stability analysis with the results of our computer simulations.

The growth rate of the qth mode of the fluctuations from the uniform state, $w(q)$, can be found by solving the appropriate characteristic equation

$$\det[L - w(q)I] = 0. \tag{10}$$

Here, I is an identity matrix and the matrix L is obtained by the linearization of Eqs. (7) and (9) for the qth mode of the fluctuations of φ and h (from $\tilde{\varphi}$ and $\tilde{h}$, respectively), leading to the following expression:

$$L = \begin{bmatrix} M_\varphi[-\gamma_\varphi q^4 + q^2(2a_{20} - \kappa H_0^2)] - \Gamma & -M_\varphi q^4 \kappa H_0 \\ -M_h \kappa H_0 q^2 + \Gamma\xi & -M_h(\kappa q^4 + q^2\sigma) \end{bmatrix}. \tag{11}$$

The roots of characteristic equation (10) are given by $w(q) = \frac{1}{2}[\mathrm{Tr}(L) \pm \sqrt{\mathrm{Tr}(L)^2 - 4\det(L)}]$ and define the stability of the uniform solution. If, for the given system parameters, $\mathrm{Re}[w(q)] < 0$ for any value of q [see, for example, Fig. 1(a), dashed line], then the uniform solution $(\tilde{h} \equiv 0, \tilde{\varphi} \equiv 0)$ is stable and any fluctuations from this solution decay with time. If $\mathrm{Re}[w(q)] > 0$ and $\mathrm{Im}[w(q)] = 0$ for some values of the wave number $q \neq 0$, then stationary Turing-like patterns are expected to occur. An example of the plot of $w(q)$ for the latter case is shown in Fig. 1(a) (solid line). All the fluctuations with wave numbers between q_1 and q_2 [as marked in Fig. 1(a)] will grow in such a system, and the late-time characteristic length scale is defined by a value of q that lies in the interval between q_1 and q_2.

If $\mathrm{Re}[w(q)] > 0$ and $\mathrm{Im}[w(q)] \neq 0$ at some values of $q \neq 0$ [see Fig. 1(b)], then traveling waves are expected to be observed in the system. Fluctuations with wave numbers between q_1 and q_2 [as marked in Fig. 1(b)] will grow in such a system.

The wave bifurcation line, or $\{\mathrm{Re}[w(q)] = 0, \mathrm{Im}[w(q)] \neq 0\}$, delineates the region in phase space where traveling waves are expected. The condition for this bifurcation is obtained by requiring $\mathrm{Tr}(L) = 0$ and $\mathrm{Det}(L) < 0$. This line can be

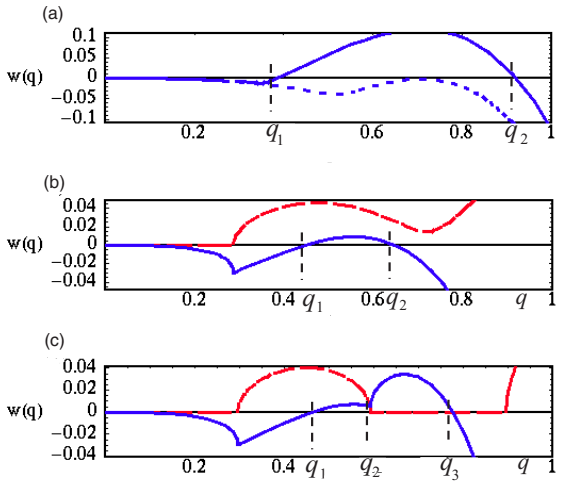

FIG. 1. (Color online) (a) $\mathrm{Re}[w(q)]$ for $\Gamma = 0.126$ (solid curve) and 0.25 (dashed curve); here, $\xi = 0$. (b) $\mathrm{Re}[w(q)]$ (solid curve) and $\mathrm{Im}[w(q)]$ (dashed curve) for $\Gamma = 0.126$ and $\xi = 6$. (c) $\mathrm{Re}[w(q)]$ (solid curve) and $\mathrm{Im}[w(q)]$ (dashed curve) for $\Gamma = 0.13$ and $\xi = 4.8$. The other parameters here and in all the simulation results below (unless specified otherwise) are $H_0 = 0.2$, $\chi = 0.5$, $\sigma = 0.05$.

expressed in terms of the critical values of the reaction rate coefficients as $\Gamma = \Gamma_1^{crit}$, with the additional condition that $\Gamma > \Gamma_2^{crit}$, where the value of Γ_2^{crit} is defined further below. Here, we define Γ_1^{crit} in such a way that, for $\Gamma = \Gamma_1^{crit}$, the condition $\mathrm{Tr}(L) = 0$ is satisfied for a nonzero value of q. More specifically, Γ_1^{crit} can be rewritten through the system parameter as

$$\Gamma_1^{crit} = M_\varphi \frac{(-2a_{20} + H_0^2\kappa + \sigma)^2}{4(\gamma_\varphi + \kappa)} \tag{12}$$

for $\xi > \xi^{crit}$, where ξ^{crit}, in turn, is defined from the condition $\Gamma_1^{crit} = \Gamma_2^{crit}$; we discuss both Γ_2^{crit} and ξ^{crit} in detail below. We note that, for the case of $\sigma = 0$, the condition in Eq. (12) reduces to the expression given in Ref. [13]. We note that in Eq. (12) and in all the following calculations, for simplicity we set $M_H = M_\varphi$.

If the reaction rate coefficient is sufficiently high, i.e., $\Gamma > \Gamma_1^{crit}$ (and $\xi > \xi^{crit}$), then the components are completely intermixed and the flat, uniform solution is stable. If, on the other hand, $\Gamma < \Gamma_1^{crit}$, then the system forms distinct patterns, as we illustrate below. Equation (12) clearly shows that an increase in the value of σ, the surface tension of the membrane, leads to a decrease in the critical value of the reaction coefficient, Γ_1^{crit}. [The latter statement is valid if $\sigma < (2a_{20} - H_0^2\kappa)$, which in turn is always valid for the parameters we used throughout these studies.] In other words, an increase in the membrane's surface tension increases the phase space where the flat, intermixed membrane is stable.

The second critical value of the reaction coefficient, Γ_2^{crit}, can also be found analytically from the condition that $\mathrm{Det}(L) = 0$, but the full expression is cumbersome; therefore, here we provide an approximate expression, which is valid for small values of σ. [We note that all of the following

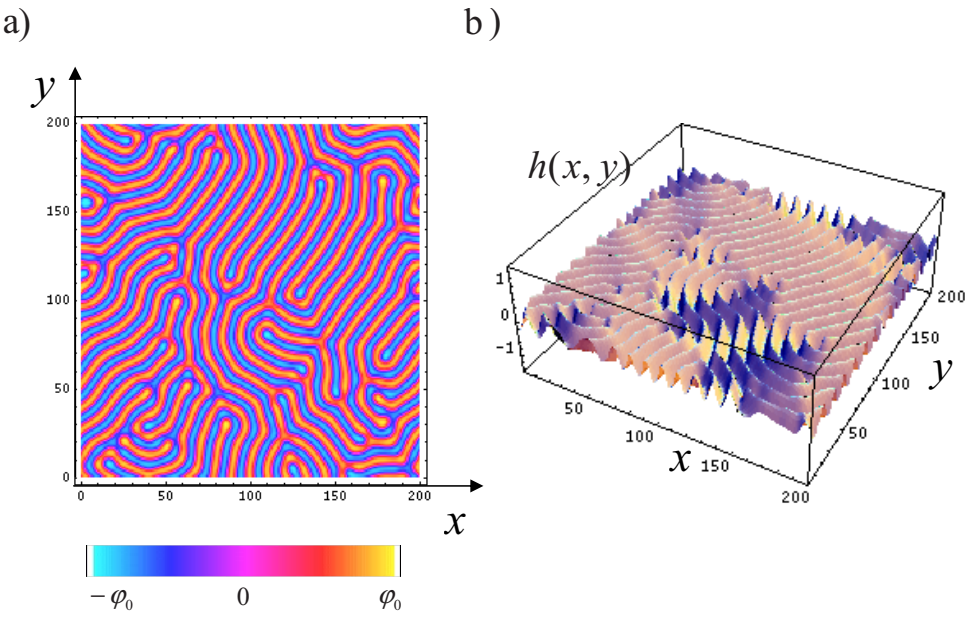

FIG. 2. (Color online) (a) Order parameter distribution within the membrane according to the scale bar with $\varphi_0=0.69$ at the simulation time step $t=2\times10^4$. (b) The height of the membrane for the same run (and same simulation time) as in (a). Here, $\Gamma=0.126$ and $\xi=0$.

conditions should be satisfied in order for this expansion in terms of σ to be valid: $\sigma \ll 1$, $\sigma \ll H_0$, and $\sigma \ll \kappa$.] This expression reads

$$\Gamma_2^{crit} \approx M_\varphi \left(\frac{a_{20}^2}{\gamma_\varphi (1+H_0\xi)} + \frac{\sigma H_0 [\xi a_{20} - H_0 \kappa (1+H_0\xi)]}{\kappa (1+H_0\xi)^2} - \frac{\sigma^2 H_0 \gamma_\varphi \{\xi a_{20} - H_0 [a_{20}\xi^2/4 + \kappa (1+H_0\xi)]\}}{a_{20}\kappa^2 (1+H_0\xi)^3} \right). \tag{13}$$

Finally, in Fig. 1(c), we plot Re$[w(q)]$ (solid line) and Im$[w(q)]$ (dashed line) for the most complicated scenario. Here, fluctuations with wave numbers between q_1 and q_2 [as marked in Fig. 1(c)] will grow {Re$[w(q)]>0$}; for these fluctuations, Im$[w(q)]\neq 0$, therefore, we expect to observe traveling waves with the characteristic wavelength $q \in [q_1, q_2]$. In addition, fluctuations with wave numbers between q_2 and q_3 [see Fig. 1(c)] will grow as well. For these fluctuations, however, Im$[w(q)]=0$ and hence we expect to see the stationary Turing-like patterns with the characteristic wavelength $q \in [q_2, q_3]$. Therefore, for reactive membranes characterized by the parameters in Fig. 1(c), we expect to observe the interaction between the stationary Turing-like and traveling wave modes. While individual bifurcations and patterns that emerge from the interactions between the Hopf and Turing or Hopf and traveling wave modes have been analyzed in detail for a wide variety of reaction-diffusion systems (see, for example, Refs. [24–27]), the interactions between the stationary Turing and the wave modes have received much less attention [28]. For example, one of the first studies of the interaction between the stationary Turing and wave instabilities was conducted only a couple of years ago by Yang *et al.* [28] for the Brusselator and Oregonator models and uncovered a large variety of spatiotemporal patterns, including modulated Turing structures and combinations of Turing structures and spiral waves. In our study, we pinpoint the parameter region where the interactions between the Turing-like and wave modes in reactive membranes can be observed, and below provide examples of such structures.

Summarizing this section, we note that the expressions for the critical values of the reaction rate constants given above [see Eqs. (12) and (13)] allow us to calculate phase diagrams and therefore to predict the behavior of such two-component reactive membranes, as well as to obtain insight into the behavior of the three-component membrane, as we illustrate further below. To facilitate the discussion, prior to detailed studies of the phase behavior, we show a few representative scenarios of the dynamics in such two-component reactive systems. In particular, the parameters used in the above calculations serve as the input to the numerical simulations; in this manner, we can visualize the morphologies of the predicted structures. We note that in Sec. III C we show that the phase diagrams obtained from the analytical calculations show excellent agreement with the phase diagrams obtained using the numerical simulations.

B. *AB* reactive film: Simulation results

Figure 2 shows an example of the Turing-like patterns in the *AB* reactive membrane; Fig. 2(a) shows the spatial distribution of the order parameter φ in the xy plane, with the relevant scale bar given below the image, and Fig. 2(b) shows the height of the membrane, $h(x,y)$, for the same run (and the same simulation time step). For initial conditions in our simulations, we choose a flat membrane $[h(x,y)=0]$ with the A and B components mixed $[\langle \varphi(x,y) \rangle = 0]$, i.e., the initial order parameter distribution was taken as a random fluctuation around zero, with the standard deviation taken to be equal to 0.05 (unless specified otherwise). The same parameters that were used to calculate the growth rate $w(q)$ in Fig. 1(a) (see solid line) were also used to generate the simulated structure in Fig. 2. According to the analytical predictions, fluctuations with wave numbers between q_1 and q_2 [see Fig. 1(a)] grow in such a system, and the characteristic length scale at late times (i.e., the width of the lamellalike domains

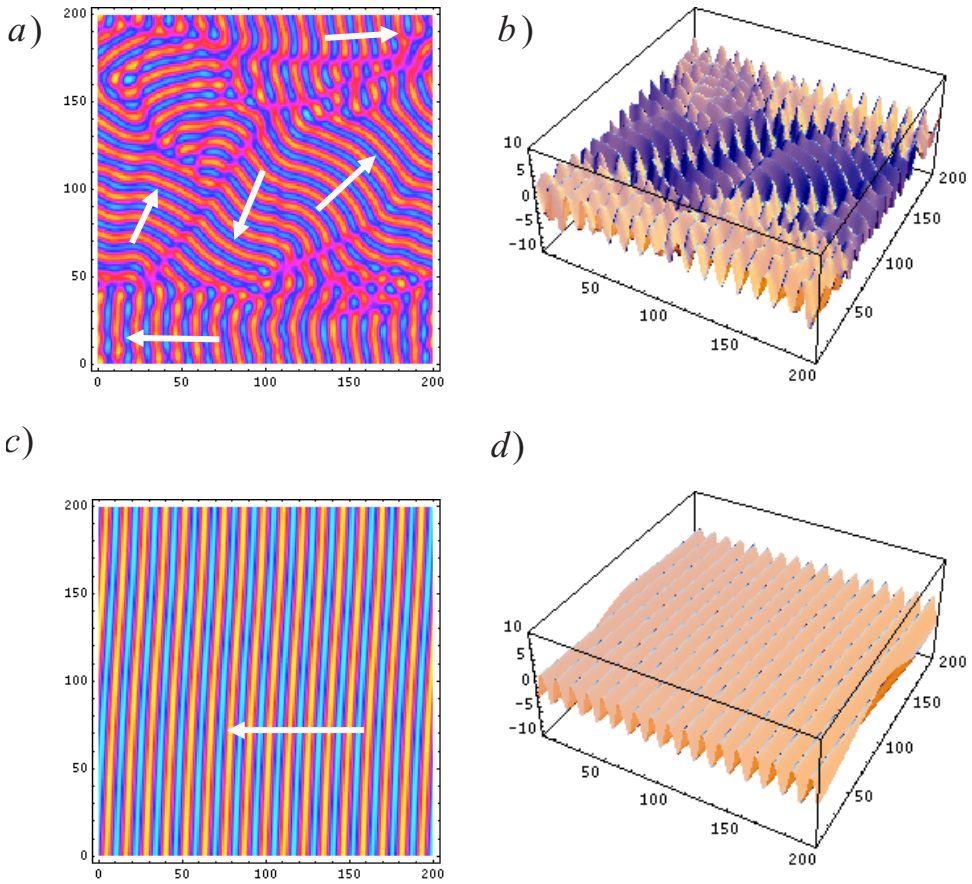

FIG. 3. (Color online) (a), (c) Order parameter distributions according to the scale bar in Fig. 2(a) with $\varphi_0=0.35$ for (a) and $\varphi_0=0.28$ for (c) at simulation time steps $t=5\times10^3$ and 4×10^4, respectively. (b), (d) The height of the membrane for the same runs and simulation time steps as in (a), (c), respectively. Here, $\Gamma=0.126$ and $\xi=6$. For these parameters, $\Gamma_1^{crit}=0.144\,15$ and $\Gamma_2^{crit}=0.1244$.

in Fig. 2), is defined by a value of q that lies within the range of $[q_1,q_2]$. We note that the patterns in Fig. 2 look identical to the patterns observed in Ref. [12], despite the fact that we used a nonzero value of the surface tension of the membrane. The surface tension, however, affects the amplitude of the undulations of the membrane height, while it does not affect the characteristic length scale. We arrived at the latter conclusion by performing a series of simulations with different values of σ. Additional simulations also show that, the higher the value of σ, the smaller the amplitude of the height undulations. However, as we discuss in the next section, the most pronounced effect of the surface tension is on the position of the phase boundaries on the phase diagrams. And, finally, we note that in this example of the Turing-like pattern, as well as in the following examples, an increase in the value of Γ increases the intermixing in the system, i.e., decreases both the bulk value of the order parameter and the characteristic width of the stripes.

Figure 3 illustrates an example of the traveling waves in the AB reactive membrane. Figures 3(a) and 3(c) show the spatial distribution of the order parameter φ in the xy plane, and Figs. 3(b) and 3(d) show the height of the membrane, $h(x,y)$, for the respective runs, at relatively early and late times. At early to intermediate times, we observe different domains traveling in different directions [see the white arrows marking the directions of propagation of the different domains in Fig. 3(a)]. At later times, these domains become more and more coherent, until the whole sample basically consists of a single coherent domain, i.e., a set of parallel stripes, traveling at a constant speed in a specific direction [for example, from right to left in Fig. 3(c)]. For the examples shown in Figs. 3(a)–3(d), we used the same parameters as we used to calculate the growth rate $w(q)$ in Fig. 1(b); i.e., here $\Gamma=0.126$ and $\xi=6$. The width of the traveling lamellar stripes is defined by a value of q that lies within the interval between q_1 and q_2 [see Fig. 1(b)].

More "exotic" scenarios of traveling waves are illustrated in Fig. 4, where we took the value of Γ to be very close to the value of Γ_1^{crit}, causing the A and B components to be quite highly intermixed; i.e., the maximum value of the order parameter is low, $\varphi_0=0.09$. Figures 4(a) and 4(b) show the respective snapshots of the spatial distribution of the order parameter φ and the height of the membrane at a fixed time step (taken at late times); here, we choose $\Gamma=0.143$ and $\xi=8$. This dynamic structure results from a superposition of different domains of traveling waves. The time evolution of the order parameter distribution along the x direction at a fixed value along the y direction ($y=10$) is shown in Fig. 4(c). We emphasize that the actual realization of such a class of dynamic structures strongly depends on the random seed in the initial order parameter distribution, as well as on the size of the sample.

For example, for the same parameters as in Fig. 4(a) but a different random seed, we can observe dynamic structures with similar features but with different morphologies and topologies. The dependence on the random seed is illustrated in Figs. 4(c)–4(e), in which we plot the evolution of the order parameter distribution at $y=10$ along the x direction. Figure 4(c) illustrates the time evolution of the order parameter along the marked dashed line for the simulation shown

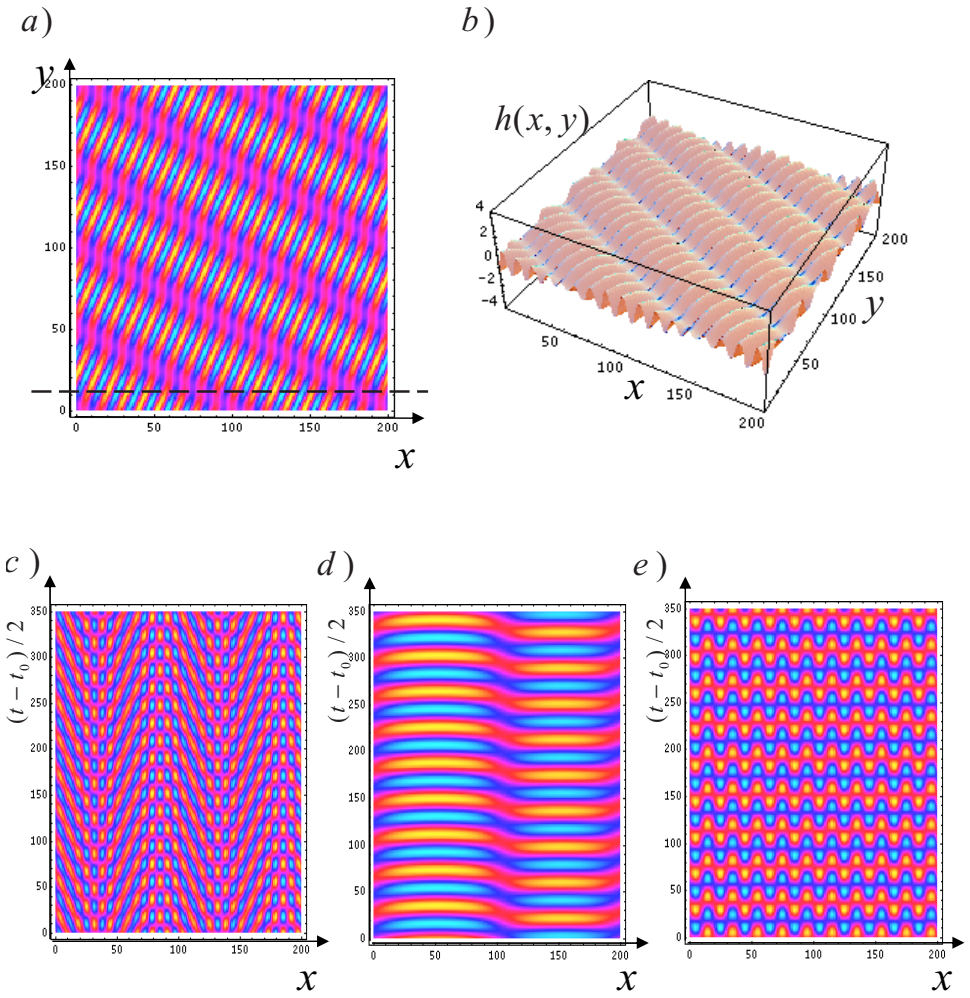

FIG. 4. (Color online) (a), (b) Order parameter distribution and the height of the membrane, respectively, at $t=406\ 16$ for the system with $\Gamma=0.143$ and $\xi=8$. For these parameters, $\Gamma_1^{crit}=0.144\ 15$ and $\Gamma_2^{crit}=0.1067$. (c)–(e) Evolution of order parameter distribution along the x direction at fixed $y=10$. All three examples have the same parameters as in (a) and (b). The difference between the runs is the different values of the initial random seed in the order parameter distribution, which was taken as a random fluctuation around its average value $\langle\varphi\rangle=0$, with standard deviation equal to 0.05. The evolution is shown at late times, where $t_0=1.1\times10^5$ and $\varphi_0=0.09$ [the scale bar is given in Fig. 2(a)] in (a), (c), (d), and (e).

in Fig. 4(a). In Figs. 4(d) and 4(e), all the parameters are the same as in Fig. 4(c), with the only difference being the value of the random seed in the initial fluctuations. The plots of the time evolution in Figs. 4(c)–4(e) illustrate the differences between the spatiotemporal patterns that appear in the same system but with different initial conditions. We also note that we observed the same dynamic behavior (i.e., similar patterns, as well as the same strong dependence on the initial random seed) for different values of ξ, provided that the reaction rate coefficient is close to Γ_1^{crit}; we will point out the relevant region on the phase diagram in the next section.

Finally, the last example (see Fig. 5) illustrates the scenario where the amplitude of the initial random fluctuations defines the final state of the system. In contrast to the previous example, where the value of the initial random seed affected the traveling wave pattern within the system, in the current example, the amplitude of the initial fluctuation defines whether traveling or stationary patterns will appear in the system. In Fig. 5, we set $\Gamma=0.13$, $\xi=4.8$, and choose the initial order parameter distribution as a random fluctuation around the completely mixed state, with the standard deviation equal to 0.05 and 0.3 for the cases in Figs. 5(a) [5(b)] and 5(c) [5(d)], respectively. In the first example {Figs. 5(a) [5(b)]}, we observe a stationary Turing-like pattern. In contrast, in the second simulation example {Figs. 5(c) [5(d)]}, we observe a complex and rather disordered dynamic structure. We note that the intermixing is higher in Fig. 5(a) than in Fig. 5(c) [$\varphi_0=0.2$ in Fig. 5(a) and $\varphi_0=0.33$ in Fig. 5(c)]. From observations of the temporal evolution of the morphology and the height variations shown in Figs. 5(c) and 5(d), we conclude that this sample effectively consists of two types of region. (Such a division into different regions is somewhat ambiguous since there is no sharp boundary between these regions and they transform into one another with time; the distinctions are made only to make the following explanation of the dynamics more clear.) Within one region, the components are highly intermixed and remain stationary for some time. Within the other region, we observe traveling waves; here, the intermixing is smaller and sets the scale ($\varphi_0=0.33$) for the whole sample.

For Fig. 5, we took the same system parameters as we used to calculate the growth rate $w(q)$ in Fig. 1(c). For these parameters, there is a region of wave numbers q $\{q\in[q_1,q_2]$; see Fig. 1(c)$\}$, where $\mathrm{Re}[w(q)]>0$ and $\mathrm{Im}[w(q)]\neq0$; therefore, traveling waves with characteristic wave numbers within this region are expected to be observed. There is also a region of higher wave numbers q $\{q\in[q_2,q_3]$; see Fig. 1(c)$\}$, where $\mathrm{Re}[w(q)]>0$ but $\mathrm{Im}[w(q)]=0$; therefore, we expect to observe stationary Turing-like patterns with a characteristic wave number within this region. In other words, according to the above linear stability analysis, we can expect to observe either traveling waves, or

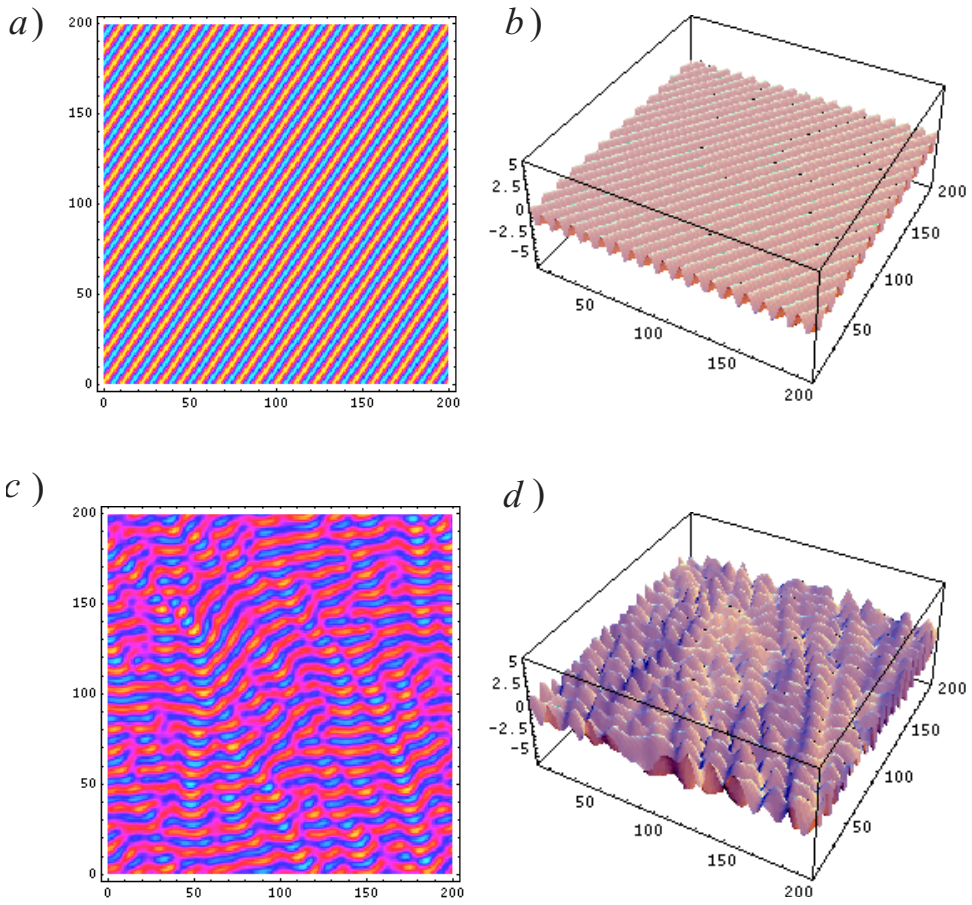

FIG. 5. (Color online) (a), (b) Stationary order parameter distribution and the height of the film, respectively, for the system with $\Gamma=0.13$ and $\xi=4.8$; here, $\varphi_0=0.20$ [the scale bar is given in Fig. 2(a)] and $t=4\times10^5$. The initial order parameter distribution was a random fluctuation around its average value $\langle\varphi\rangle=0$, with the standard deviation taken to be equal to 0.05. (c), (d) Order parameter distribution and the height of the film, respectively, at $t=2\times10^5$ for the system with the same parameters as in (a), (b); here, $\varphi_0=0.33$ and the initial order parameter distribution was a random fluctuation around $\langle\varphi\rangle=0$ with the standard deviation taken to be equal to 0.3.

stationary Turing-like patterns, or the interaction of the Turing-like and wave modes. Results of our computer simulations (Fig. 5) are in agreement with the above predictions of the linear stability analysis. In addition, the simulations give us further insight into this behavior, namely, we found that, if the initial fluctuations of the order parameter are small, we observe stationary Turing-like patterns [as in Figs. 5(a) and 5(b)]. Interestingly, we observe that stationary Turing-like patterns for the latter parameters are always aligned along a single direction. On the other hand, if initial fluctuations of the order parameter are large, we observe structures that comprise both stationary patterns and traveling waves [as in Figs. 5(c) and 5(d)]. According to our observations, the above dependence of the final structure on the initial fluctuations is robust; we repeated the runs in Fig. 5 for four different values of the random seeds (but keeping the same amplitude of the initial fluctuation of the order parameter) and obtained qualitatively the same structures.

C. Phase diagrams

In this section, we plot the phase diagrams and compare the analytical predictions with the results of our computer simulations. Figure 6 shows the phase diagram in the $\Gamma\xi$ plane. The solid (blue online) curve is the $\Gamma=\Gamma_2^{crit}(\xi)$ curve; along this curve, $\mathrm{Re}[w(q)]=0$ and $\mathrm{Im}[w(q)]=0$. If $\Gamma<\Gamma_2^{crit}(\xi)$ {and therefore $\mathrm{Re}[w(q)]>0$ and $\mathrm{Im}[w(q)]=0$}, the system exhibits stationary Turing-like patterns [see solid line, Fig. 1(a)]. The dashed (red) line in Fig. 6 is the $\Gamma=\Gamma_1^{crit}(\xi)$ line. Along this wave bifurcation line, $\mathrm{Re}[w(q)]=0$ and $\mathrm{Im}[w(q)]\neq0$ for some range of values of q. If $\Gamma<\Gamma_1^{crit}(\xi)$ {and therefore $\mathrm{Re}[w(q)]>0$ and $\mathrm{Im}[w(q)]\neq0$}, the system exhibits traveling waves, as in the example shown in Fig. 1(b). The various discrete symbols mark the observed locations of the uniform, flat solution (filled boxes), oscillations in space (i.e., stationary Turing-like patterns) (open diamonds), or oscillations in both space and time (filled circles). Each data point represents three independent runs; in all the runs, the initial order parameter distribution was taken as a

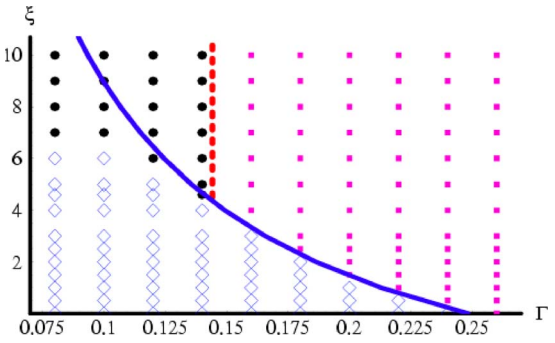

FIG. 6. (Color online) Phase diagram in the Γ, ξ plane; $\Gamma=\Gamma_1^{crit}(\xi)$ along the dashed (red online) line and $\Gamma=\Gamma_2^{crit}(\xi)$ along the solid (blue) curve. Each simulation data point represents three independent runs. Filled boxes represent the uniform, flat solution, open diamonds represent stationary Turing-like patterns, and filled circles represent oscillations in both space and time.

random fluctuation around the completely mixed state, with the standard deviation taken to be equal to 0.05. We note that, for zero surface tension, the analytically obtained phase diagram in the $\Gamma\xi$ parameter space was given in Ref. [13]. The presence of the nonzero surface tension decreases the region where the traveling waves can be observed and shifts this region to lower values of Γ and higher values of ξ.

Figure 6 shows that, for the small values of ξ, namely, $\xi < \xi^{crit}$, where ξ^{crit} is defined from $\Gamma_2^{crit}(\xi^{crit})=\Gamma_1^{crit}$, one can observe either the flat uniform state [for $\Gamma \geqslant \Gamma_2^{crit}(\xi)$] or the stationary Turing-like patterns [for $\Gamma < \Gamma_2^{crit}(\xi)$]. The traveling wave solution is observed only if the direct coupling between the reaction and the shape changes is sufficiently strong (i.e., $\xi \geqslant \xi^{crit}$). In the latter case, only traveling waves are observed in the system if the reaction rate coefficient satisfies the condition $\Gamma_2^{crit}(\xi) \leqslant \Gamma < \Gamma_1^{crit}$. The most common example of the traveling wave structure is given in Fig. 3. Within the same region, but very close to the bifurcation line $\Gamma=\Gamma_1^{crit}$, a variety of the more exotic traveling wave patterns can occur. An example of these structures is shown in Fig. 4; the actual realization depends on the initial conditions. For such exotic patterns, the intermixing is very high, i.e., $\varphi \ll 1$.

We found that traveling waves can also occur if $\Gamma \leqslant \Gamma_2^{crit}(\xi)$ at relatively high values of ξ [see filled circles on the left of the $\Gamma_2^{crit}(\xi)$ curve in Fig. 6]. We note that this region of the phase diagram [namely, the region where $\Gamma < \Gamma_2^{crit}(\xi)$ and $\xi \geqslant \xi^{crit}$] represents the region at which both the traveling wave and Turing-like modes interact. As we have noted earlier, the interaction between the traveling waves and Turing-like patterns were studied less than the interaction between any other different bifurcations [28]. For intermediate values of ξ within this region (where the transition between the Turing-like and wave patterns occur), an increase in the amplitude of the initial fluctuation of the order parameter can lead to the appearance of traveling waves instead of the Turing-like structure at such "boundary" points. For example, at the boundary point $\xi=6$ and $\Gamma=0.1$ (for the case shown in Fig. 6), we observe traveling waves in all four additional independent runs when we choose the standard deviation of the order parameter equal to 0.3 (instead of stationary Turing-like patterns as marked in Fig. 6, where the initial standard deviation was equal to 0.05). We emphasize that the late-time dynamic state of the system strongly depends on the initial fluctuations only at these points of the phase diagram (i.e., at the boundary points in the region where the Turing-like and wave structures interact) or close to the traveling wave bifurcation line (see Fig. 4). In all the other points on the phase diagram, large changes in the amplitude of the initial fluctuations of either the order parameter or the height of the membrane do not affect the late-time dynamics or stationary structures. Additional simulations showed that, for example, variations in the initial conditions for the Turing-like structures affects only the position of the lamellar stripes, but does not affect their width, height, or the effective intermixing within the system.

The phase diagram in Fig. 6 reveals an important feature of the system's dynamic behavior: for the reactive rate coefficients considered here, traveling waves can be observed only if $\xi \geqslant \xi^{crit}$. Hence, it is of interest to determine how ξ^{crit} depends on the characteristics of the membrane. To address this issue, in Fig. 7 we plot the dependence of ξ^{crit} on the spontaneous curvature H for different values of the membrane surface tension and bending elasticity. For each set of parameters, we found the value of the ξ^{crit} by numerically solving the equation $\Gamma_2^{crit}(\xi^{crit})=\Gamma_1^{crit}$, where we first used the full (nonasymptotic) expression for $\Gamma_2^{crit}(\xi^{crit})$ and then we checked that the asymptotic expression [Eq. (13)] gives the identical results for the same parameters.

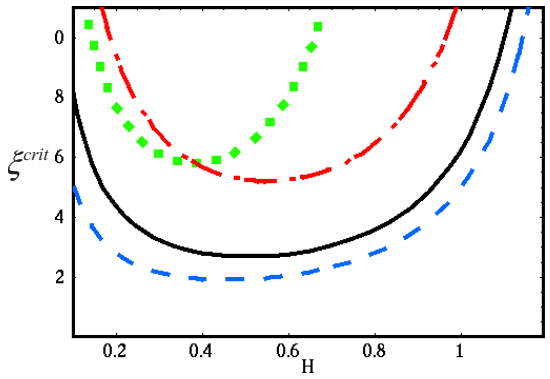

FIG. 7. (Color online) Dependence of ξ^{crit} on the spontaneous curvature H_0. Here, $\kappa=0.5$, $\sigma=0.05$ for the solid curve, $\kappa=0.5$, $\sigma=0$ for the dashed (blue online) curve, $\kappa=0.5$, $\sigma=0.15$ for the dot-dashed (red online) curve, and $\kappa=1$, $\sigma=0.05$ for the dotted (green online) curve.

The solid curve in Fig. 7 shows $\xi^{crit}(H)$ for the reference parameters we used in the above simulations (i.e., $\sigma=0.05$ and $k=0.5$); more specifically, the point on this curve at $H=0.2$ gives the ξ^{crit} that is an intersection of $\Gamma_2^{crit}(\xi)$ and Γ_1^{crit} in the phase diagram shown in Fig. 6. The dashed and the dot-dashed curves in Fig. 7 represent $\xi^{crit}(H)$ for zero and for relatively high ($\sigma=0.15$) surface tension, respectively. One can see that the functional dependence of $\xi^{crit}(H)$ is the same for both these limits; that is, $\xi^{crit}(H)$ decreases for small H and increases for higher H, with the minimum located approximately at $H \approx 0.6$. However, the increase in surface tension leads to an increase in absolute value of the ξ^{crit}.

The dotted curve in Fig. 7 is for the case where $\sigma=0.05$ and $k=1$. By comparing this curve with the solid curve (where $\sigma=0.05$ and $k=0.5$), we see that an increase in the bending modulus k not only leads to a strong increase in the value of the ξ^{crit}, but also shifts the value of H at which the $\xi^{crit}(H)$ curve has a minimum to a much lower value.

The above dependencies of ξ^{crit} on the system parameters have a clear physical interpretation; namely, it is more difficult to generate traveling waves in stiffer membranes (higher k) or membranes with higher surface tension. Consequently, higher values of ξ (i.e., stronger coupling between the reaction and the shape of film) are needed for the traveling waves to occur.

Finally, in Fig. 8 we plot the phase diagram in the Γ, σ parameter space for a fixed value of $\xi=5$. Here, the solid (blue) curve corresponds to $\Gamma=\Gamma_2^{crit}(\sigma)$ and the dashed (red) line corresponds to $\Gamma=\Gamma_1^{crit}(\sigma)$. As in Fig. 6, the various discrete symbols mark the observed locations of the uniform,

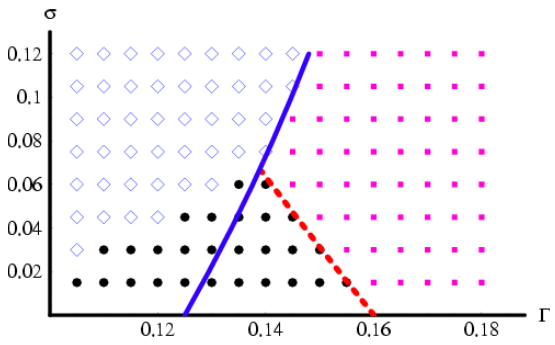

FIG. 8. (Color online) Phase diagram in the Γ, σ plane. $\Gamma=\Gamma_1^{crit}(\sigma)$ along the dashed (red online) line and $\Gamma=\Gamma_2^{crit}(\sigma)$ along the solid (blue) curve. Each simulation data point represents three independent runs. Filled boxes represent the uniform, flat solution, open diamonds represent stationary Turing-like patterns, and filled circles represent oscillations in both space and time.

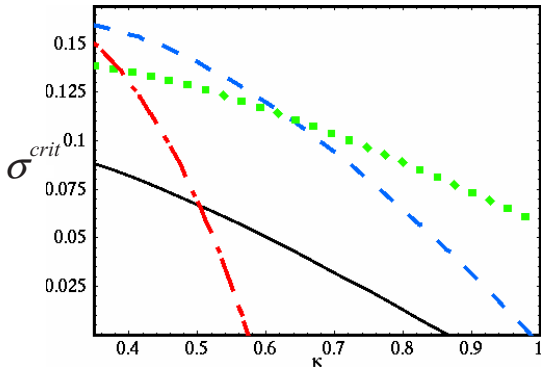

FIG. 9. (Color online) Dependence of σ^{crit} on the bending elasticity κ. Here, $H_0=0.2$, $\xi=5$ for the solid curve, $H_0=0.5$, $\xi=5$ for the dashed (blue online) curve, $H_0=0.9$, $\xi=5$ for the dot-dashed (red online) curve, and $H_0=0.2$, $\xi=8$ for the dotted (green online) curve.

flat solution (filled boxes), oscillations in space (open diamonds), or oscillations in both space and time (filled circles). Again, each data point represents three independent runs. Figure 8 illustrates that, for the relatively large values of σ, such that $\sigma>\sigma^{crit}$, the system forms only Turing-like patterns [for $\Gamma<\Gamma_2^{crit}(\sigma)$] or the flat, uniform state [for $\Gamma\geqslant\Gamma_2^{crit}(\sigma)$]. Here, we define the critical value of the interfacial tension σ^{crit} from $\Gamma_1^{crit}(\sigma^{crit})=\Gamma_2^{crit}(\sigma^{crit})$.

Figure 8 also illustrates that for smaller values of σ (i.e., for $\sigma\leqslant\sigma^{crit}$), and for $\Gamma\geqslant\Gamma_2^{crit}(\sigma)$, we can observe either traveling waves if $\Gamma<\Gamma_1^{crit}(\sigma)$ or a mixed flat state if $\Gamma\geqslant\Gamma_1^{crit}(\sigma)$. Finally, if $\sigma\leqslant\sigma^{crit}$ and $\Gamma<\Gamma_2^{crit}(\sigma)$, according to the linear stability analysis, we can expect both Turing-like patterns and traveling waves. The simulation results show that for the relatively small values of σ within this region, traveling waves are generated (filled circles in the left region of the phase diagram in Fig. 8), while for the relatively high values of σ, we observe stationary Turing-like patterns (open diamonds in the left region of the phase diagram). It is only for the values of σ on the boundary between these two regions that we observe more complicated behavior, i.e., a strong dependence of the final dynamical structure on the amplitude of the initial fluctuation, similar to the scenario described in Fig. 5. We note that in all the presented results (i.e., see Figs. 6 and 8), $\Gamma_1^{crit}>\Gamma_2^{crit}$ [29]. In other words, if the region with the traveling waves exists in the parameter space, it is always located next to the region in which the flat completely intermixed membrane is stable, for all the system parameters considered in this work. Therefore, the continuous decrease in the value of Γ, starting from some very high value (keeping all other parameters fixed), will drive the system from the flat intermixed state to the state in which only traveling waves can be observed, and only then to the state in which both traveling waves and Turing-like patterns can occurs.

The critical value of the lateral surface tension, σ^{crit}, can be obtained analytically using Eqs. (11) and (12); however, since the expression for σ^{crit} is cumbersome, we only provide the functional dependence of σ^{crit} on the bending modulus κ for different vales of H_0 and ξ (see Fig. 9). The solid and dotted curves in Fig. 9 correspond to the values of $\xi=5$ and 8, respectively, while the value of H_0 is fixed in both cases at $H_0=0.2$. A comparison of these two curves provides a clear physical interpretation of the data: the higher the value of ξ, the larger the parameter space for which traveling waves can be observed. In other words, for relatively high ξ, traveling waves can be observed in membranes with relatively high surface tensions and with relatively high bending elasticity moduli. Moreover, if the value of ξ is constant (here, we choose $\xi=5$), but the spontaneous curvature is increased moderately (from $H_0=0.2$ for the solid curve to $H_0=0.5$ for the dashed curve), the traveling waves can also be observed in membranes with higher surface tension and with higher bending elasticity modulus. However, if the spontaneous curvature is increased even further (see dot-dashed curve, for which $H_0=0.9$), the traveling waves can be observed for relatively high surface tension, but only for very flexible membranes.

To summarize, we detailed the behavior of reactive binary membranes for different system parameters. In particular, we defined critical values of σ^{crit} below which traveling waves could be observed in the system. In addition, we pinpointed the regions in the phase diagram where the late-time dynamic state of the system can strongly depend on the initial fluctuations. In the next section, we illustrate how the dynamics of such reactive membranes are changed if we add the third, nonreactive component C into the membrane.

D. Three-component membranes

In this section, we simulate the dynamics of the three-component system. First, we note that, within the binary domains, the linear stability analysis and the diagrams of the dynamic states remain the same as given above. In the other words, we can readily use the above results to choose the specific dynamic behavior of the AB reactive component and to probe how that behavior changes with the addition of the nonreactive C component.

Figure 10 illustrates one of the examples of the evolution of the three-component membrane. As initial conditions, we choose a flat membrane with all three components being mixed, i.e., $h(x,y)=0$, $\langle\varphi(x,y)\rangle=0$, and $\langle\psi(x,y)\rangle=\psi_0$; here,

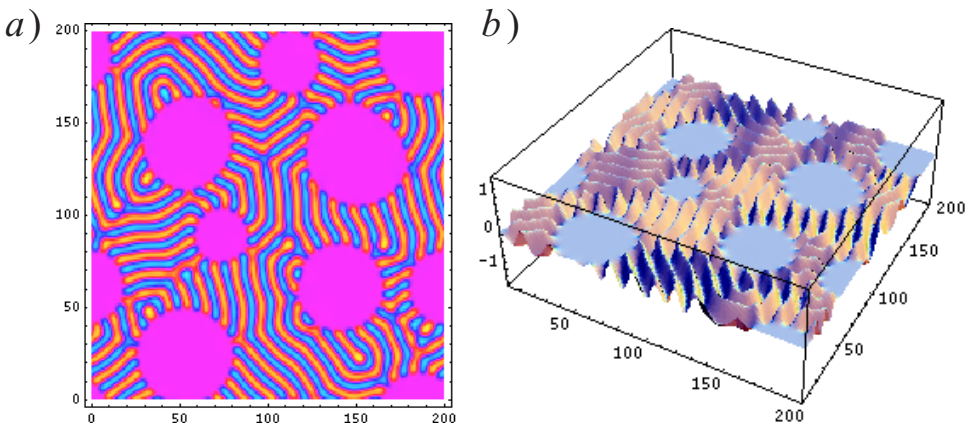

FIG. 10. (Color online) (a) Order parameter distribution within the membrane at the simulation time step $t=4\times10^4$; the A and B components are shown according to the scale bar in Fig. 2(a) with $\varphi_0=0.69$. The C component is shown in gray (pink online). (b) The height of the membrane for the same run (and the same simulation time) as in (a). Here, $\Gamma=0.126$, $\xi=0$, and the concentration of the C component is $\psi_0=0.27$.

ψ_0 is the volume fraction of the nonreactive C component (more specifically, $\psi_0=0.27$ in Fig. 10). The reaction parameters for the AB blend are chosen as $\Gamma=0.126$ and $\xi=0$; i.e., the binary AB domains correspond to the simulations shown in Fig. 2. Consequently, the composition and height patterns within the AB domains in the three-component membrane (Fig. 10) are essentially the same as in the two-component reactive membrane (Fig. 2). The only difference is that AB lamellar domains lying close to C regions now preferentially orient perpendicular to the C domains. This behavior can be understood by recalling that C is equally incompatible with both A and B, and thus presents a neutral interface to the AB stripes; it is known that lamellar layers orient perpendicular to such neutral surfaces [30]. The snapshot in Fig. 10 corresponds to intermediate times in the evolution of the membrane. At later times, the phase-separation process continues, and therefore the characteristic size of the C domain continues to grow, while the total number of the C domains decreases. The AB reactive regions are slaved to the evolution of the C domains, i.e., AB lamellae rearrange to preferentially orient perpendicular to the C interfaces at each moment of time. Due to such rearranging of the lamellar-like structures, the presence of the C component prevents the dynamics within the AB domains from freezing, which otherwise occurs in the pure AB reactive membrane.

Figure 11 provides two other examples of the evolution of the three-component membrane. In both cases in Fig. 11, the reaction parameters for the AB blend are chosen as $\Gamma=0.126$ and $\xi=6$, being the same as those used to generate Fig. 3. Thus, it is anticipated that traveling waves will appear within the sample. In Fig. 11(a) [11(b)], we again choose as initial conditions a flat membrane with all three components being mixed [i.e., $h(x,y)=0$, $\langle\varphi(x,y)\rangle=0$ and $\langle\psi(x,y)\rangle=0.27$]. The white arrows in Fig. 11(a) indicate the directions of the propagation of the traveling waves at the specific regions within the sample. Here, the traveling waves are strictly confined between the C domains. The boundaries of the C domains, however, continue to evolve due to the coarsening of the C component. The latter fact strongly affects the propagation of the traveling waves and prevents the appearance of a coherent traveling pattern, as seen in Fig. 3.

Finally, we considered the evolution of the above systems with modified initial conditions for the order parameter ψ. In particular, we assumed that the domain of C already exists at the beginning of the simulations. That is, at the center of the simulation box, we initially set $\psi(x,y)=1$ within a circle of radius $R=95$ lattice sites and set $\psi(x,y)=0$ everywhere else. The evolution at relatively late times in this case is shown in Figs. 11(c) and 11(d). The white arrows show the directions of propagation of the traveling waves in specific regions. In this example, the waves propagate from the lower left corner of the sample toward the C domain. Close to the boundary of the C domain, the AB stripes reorient perpendicular to the C domains and therefore form a checkerboard pattern along the C boundary, which meets a traveling front [see enlarged image of the part of the checkerboard pattern in the bottom inset of the Figure 11(d)]. The top inset in Fig. 11(d) illustrates the propagation of the traveling waves after the C domains. Here, the traveling patterns are seen to originate from the upper boundary of the C domain and propagate away from it. Due to the imposed periodic boundary conditions, the stripes are bent to different sides, so that defects appear along the upper diagonal of the sample. We note that the choices of a different initial random seed or different sizes of the C domain or the simulation box affect only the direction of the wave propagation throughout the sample; the main features described above (i.e., the formation of the checkerboard pattern along the boundary of the C domain, which meets a traveling front, and the appearance of traveling defects above the C domain) remains robust in all our simulations. These features are also present in the example shown in Fig. 11(a) [11(b)]; they are, however, much less distinct since the C domains are smaller and the traveling waves propagate in different directions.

IV. CONCLUSIONS

Using theory and numerical simulations, we examined the behavior of reactive, stimuli-responsive membranes, which comprise two or three components. An external stimulus initiates a chemical reaction within the membrane that interconverts two of the components, A and B, which have specified spontaneous curvatures. As noted in Refs. [12,13], such an interconversion reaction can be understood, for example, as an isomerizationlike chemical transformation, initiated by an external light. The third component C is assumed to be nonreactive and is incompatible with the A and B components. The binary part of our model is based on the model proposed by Reigada *et al.* [13]; we have, however, extended the latter

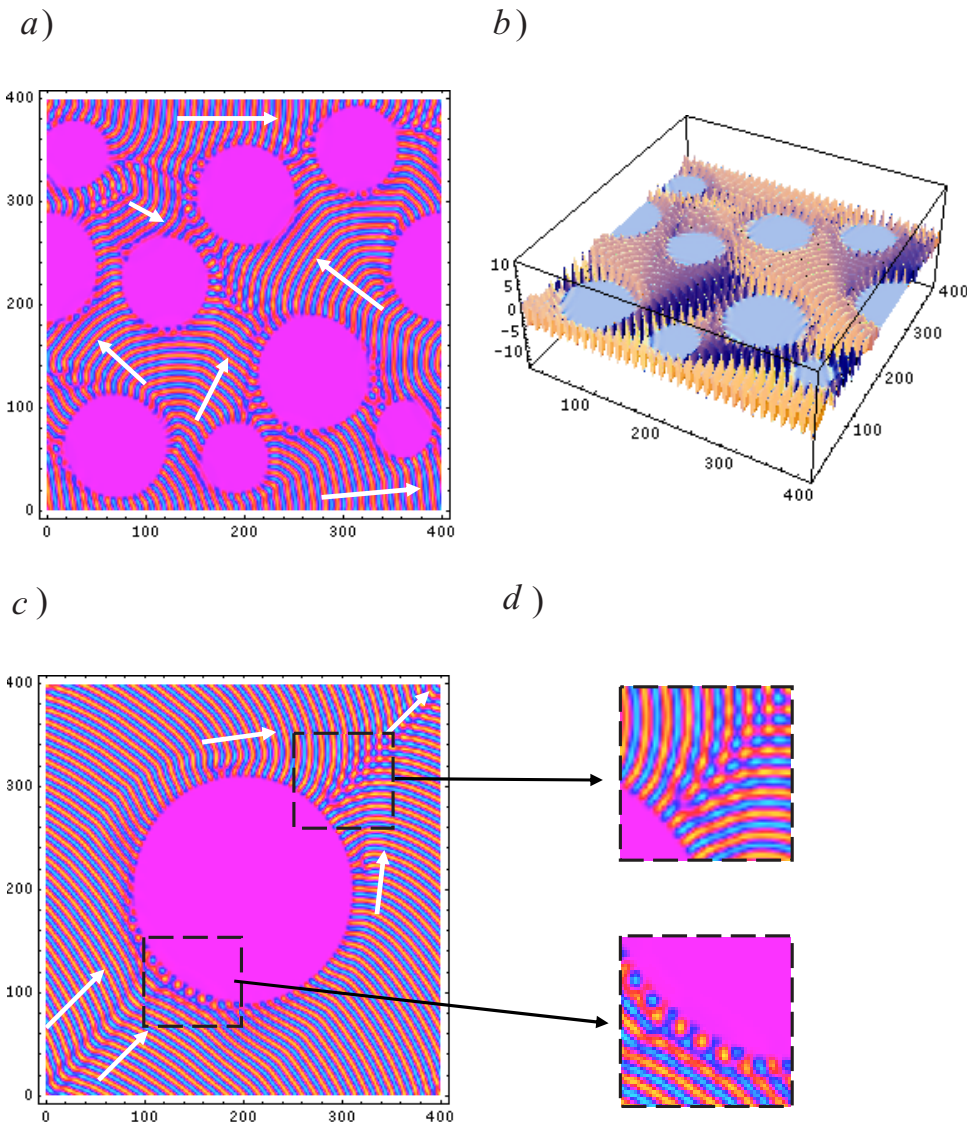

FIG. 11. (Color online) (a), (b) Order parameter distribution and the height of the membrane, respectively, at the simulation time step $t=300\,140$. The A and B components are shown according to the scale bar in Fig. 2(a) with $\varphi_0=0.28$. The C component is shown in gray (pink online). Here, $\Gamma=0.126$, $\xi=6$, and the concentration of the C component is $\psi_0=0.27$. (c), (d) Order parameter distribution and the height of the membrane, respectively, at the simulation time step $t=100\,140$. Here, $\Gamma=0.126$, $\xi=6$, and in the initial condition we choose the C component to be located within a circle of the radius $R=95$ in the center of the simulation box. In (a) and (c), the white arrows show the local directions of propagation of the traveling waves.

approach by explicitly including the effects of the lateral surface tension of the membrane. For the two-component (AB) reactive membranes, we calculated phase diagrams in terms of different parameters and showed that the surface tension of the membrane strongly affects the location of the phase boundaries. For example, we defined critical values of the lateral surface tension below which the traveling waves could be observed in the system. In addition, we pinpointed the regions on the phase diagram where the late-time behavior strongly depends on the initial fluctuations, i.e., where such a reactive system has some memory of its prior state.

For the case of the three-component reactive membrane, we illustrated how the presence of the nonreactive component affects the final dynamical patterns within the membrane. More specifically, we showed that the AB reactive domains are slaved to the evolution of the C domains, i.e., the AB patterns rearrange to preferentially orient perpendicular to the boundaries of the C domains at each moment of time. Due to the latter effect, the C component prevents the evolution within the AB domains from freezing (if such reaction parameters are chosen that stationary patterns occur within the AB regions.)

In examining the ternary systems, we also illustrated that the nonreactive C domains strongly affect the propagation of the traveling waves in the reactive membrane. This behavior can potentially be used in applications of the synthetic membranes. For example, if the C component is an impurity, a change in the dynamics or direction of the traveling waves would signal the presence of impurities in the sample. If the C domain is relatively large and if there is a small number of

such domains, it might be possible to use the change in the traveling waves dynamics to remotely track the position of the individual *C* domains within the membrane.

We also showed that the topology of the responsive, reactive membrane strongly depends on the local composition, the reaction parameters, the bending modulus, and the surface tension of the membrane. Thus, through the judicious choice of parameters, the "designer" can potentially create stationary or traveling relief patterns of desired topologies. Moreover, additional preliminary results (which will be reported in a separate study) show that the dynamics and the local topologies of such model reactive membranes strongly depend on externally induced gradients in the system, such as a spatial gradient in the reaction rate coefficients. We found that, in response to even small changes in this gradient, the reactive membrane undergoes dynamic reconstruction. In the case of the ternary membrane, it might be possible to exploit such "gradient sensing" to control the transport of the *C* component within the membrane. The behavior would permit a cleaning of the membrane if the *C* component is an impurity or targeted delivery of the *C* component to specific locations. Such gradient sensing and dynamic reconstruction will be the subjects of separate studies.

ACKNOWLEDGMENT

The authors gratefully acknowledge financial support from DOE.

[1] A. N. Parikh and J. T. Groves, MRS Bull. **31**, 507 (2006).
[2] R. Lipowsky and E. Sackmann, *The Structure and Dynamics of Membranes* (Elsevier, Amsterdam, 1995).
[3] M. Mueller, K. Katsov, and M. Schick, Phys. Rep. **434**, 113 (2006).
[4] K. John and M. Bar, Phys. Biol. **2**, 123 (2005).
[5] S. Ramaswamy, J. Toner, and J. Prost, Phys. Rev. Lett. **84**, 3494 (2000).
[6] J. B. Manneville, P. Bassereau, D. Levy, and J. Prost, Phys. Rev. Lett. **82**, 4356 (1999).
[7] J. B. Manneville, P. Bassereau, S. Ramaswamy, and J. Prost, Phys. Rev. E **64**, 021908 (2001).
[8] H. Y. Chen, Phys. Rev. Lett. **92**, 168101 (2004).
[9] C. H. Chen and H. Y. Chen, Phys. Rev. E **74**, 051917 (2006).
[10] N. Gov, Phys. Rev. Lett. **93**, 268104 (2004).
[11] P. G. Petrov, J. B. Lee, and H. G. Dobereiner, Europhys. Lett. **48**, 435 (1999).
[12] R. Reigada, J. Buceta, and K. Lindenberg, Phys. Rev. E **71**, 051906 (2005).
[13] R. Reigada, J. Buceta, and K. Lindenberg, Phys. Rev. E **72**, 051921 (2005).
[14] K. Good *et al.*, J. Chem. Phys. **121**, 6052 (2004).
[15] R. D. M. Travasso *et al.*, J. Chem. Phys. **122**, 194906 (2005).
[16] R. D. M. Travasso, O. Kuksenok, and A. C. Balazs, Langmuir **22**, 2620 (2006).
[17] F. Liu and N. Goldenfeld, Phys. Rev. A **39**, 4805 (1989).
[18] M. Bahiana and Y. Oono, Phys. Rev. A **41**, 6763 (1990).
[19] S. C. Glotzer, E. A. DiMarzio, and M. Muthukumar, Phys. Rev. Lett. **74**, 2034 (1995).
[20] J. J. Christensen, K. Elder, and H. C. Fogedby, Phys. Rev. E **54**, R2212 (1996).
[21] R. D. M. Travasso, O. Kuksenok, and A. C. Balazs, Langmuir **21**, 10912 (2005).
[22] O. Kuksenok, R. D. M. Travasso, and A. C. Balazs, Phys. Rev. E **74**, 011502 (2006).
[23] Y. Oono and S. Puri, Phys. Rev. A **38**, 434 (1988).
[24] M. C. Cross and P. C. Hohenberg, Rev. Mod. Phys. **65**, 851 (1993).
[25] A. M. Zhabotinsky, M. Dolnik, and R. Epstein, J. Chem. Phys. **103**, 10306 (1995).
[26] A. DeWit, D. Lima, G. Dewel, and P. Borckmans, Phys. Rev. E **54**, 261 (1996).
[27] M. Meixner, A. Dewit, S. Bose, and E. Scholl, Phys. Rev. E **55**, 6690 (1997).
[28] L. F. Yang *et al.*, J. Chem. Phys. **117**, 7259 (2002).
[29] There is, however, no special requirement that Γ_1^{crit} should be larger then Γ_2^{crit} for any possible system parameters. In fact, system parameters exist at which $\Gamma_2^{crit} > \Gamma_1^{crit}$. In other words, in such systems, the continuous decrease in the value of Γ (starting from some very high value) will drive the system from a flat intermixed state to a state in which only Turing-like patterns can be observed, and only then to a state in which both traveling waves and Turing-like patterns could be potentially observed.
[30] G. J. Kellogg, D. G. Walton, A. M. Mayes, P. Lambooy, T. P. Russell, P. D. Gallagher, and S. K. Satija, Phys. Rev. Lett. **76**, 2503 (1996).